



Pergamon

Available online at [www.sciencedirect.com](http://www.sciencedirect.com)

SCIENCE @ DIRECT®



Acta Materialia 51 (2003) 5319–5334

[www.actamat-journals.com](http://www.actamat-journals.com)

# Effects of pores and interfaces on effective properties of plasma sprayed zirconia coatings

Z. Wang <sup>a</sup>, A. Kulkarni <sup>b</sup>, S. Deshpande <sup>b</sup>, T. Nakamura <sup>a,\*</sup>, H. Herman <sup>b</sup>

<sup>a</sup> Department of Mechanical Engineering, State University of New York at Stony Brook, CEAS, Stony Brook, NY 11794, USA

<sup>b</sup> Department of Materials Science and Engineering, State University of New York at Stony Brook, Stony Brook, NY 11794, USA

Received 12 February 2003; received in revised form 8 July 2003; accepted 10 July 2003

## Abstract

It is difficult to establish structure–property relationships in plasma sprayed coatings because of their unique and intermingled splat microstructures incorporating networks of various intrinsic process-dependent microdefects. In this paper, these coatings are characterized using two distinctly different approaches, both based on novel experimental techniques and computational modeling tools. In each approach, detailed finite element models are illustrated to represent the porous coatings fabricated with four different types of zirconia feed powder. One approach is based on small-angle neutron scattering (SANS) studies carried out to quantify microstructure. In this approach, the pore morphology is idealized by artificially rebuilding, based on the collective microstructural information obtained in terms of component porosities of three pore systems, their opening dimensions and orientation. The other method relies on image analysis of real microstructural images obtained using scanning electron microscopy (SEM). The finite element mesh for the actual cross-sectional model, generated by thresholding the SEM images, is constructed with the object oriented finite (OOF) element method. Through these two approaches, the effective thermal conductivity and elastic modulus along the spray, as well as the transverse directions are estimated for thermally sprayed yttria-stabilized zirconia (PSZ) coatings. Our results show the effectiveness of these computational approaches for estimating material properties with each approach having its strength and weakness. However, in comparison with experimentally measured properties, there exist some limitations in both approaches. To further probe the source of discrepancy within the measurements, the coatings are thermal cycled to reduce the effect of splat boundaries on properties. Additional models are constructed for these coatings and their analysis is carried out. For the first time, the influence of the splat interfaces on the effective properties of sprayed coatings is quantified.

© 2003 Acta Materialia Inc. Published by Elsevier Ltd. All rights reserved.

**Keywords:** Plasma sprayed coatings; Porosity; Splat boundary; Small-angle neutron scattering; Thermal conductivity

## 1. Introduction

Thermally sprayed ceramic coatings have been widely used for thermal protection of air-cooled components in gas turbine engine hot sections. In this process, the feedstock powder material is

\* Corresponding author. Tel.: +1-631-632-8312; fax: +1-631-632-8544.

E-mail address: [toshio.nakamura@sunysb.edu](mailto:toshio.nakamura@sunysb.edu) (T. Nakamura).

melted and accelerated, which upon impinging the substrate, rapidly solidifies to form splats. The coating develops by successive build-up of these splats. The microstructure of these coatings is characterized by the existence of splats along with other microstructural features such as interlamellar and globular pores (due to imperfect contact and partially molten particles), intrasplat microcracks (due to stress relaxation) and splat boundaries [1]. These porous microstructures greatly influence effective properties such as thermal conductivity and elastic modulus and thus influence coating behavior.

One of the most common applications of these coatings is the insulation of substrate components as thermal barrier coatings (TBCs) [1–3]. The architecture of porosity in these coatings allows advantages in terms of cooling requirements, efficiency and life extension of components. While microstructure development of these coatings is process-dependent, there is a need to establish quantitative microstructure–property correlations for optimal design. There has been extensive analytical and numerical work in establishing quantitative relations between overall properties and microstructures for porous media. Markov and Preziosi [4] reviewed some rigorous methods to relate effective properties of random porous media through microstructure characterization via statistical correlation functions. Kaviani [5] presented a local volume averaging method for heat transfer analysis in periodic porous media. These analytical methods feature a homogenizing procedure within a *representative volume element*, which is small enough from a macroscopical point of view, but should be large enough to contain sufficient microstructural inhomogeneity. Another approach by Kachanov and co-workers [6,7] has been used in modeling the dominant elements of porous space (one parallel family and one perpendicular family of pores in this case) and estimating the effective anisotropic properties of the coatings. Leigh and Berndt [8,9] have determined the size–shape distribution of void components for a water-stabilized plasma-spray-formed  $\text{Al}_2\text{O}_3$ –13 wt%  $\text{TiO}_2$  using quantitative stereological analysis. The individual voids were assumed to be elliptical, and the quantitative information of voids was acquired in terms

of shape and size. Numerous analytical studies have been reported to evaluate the effective elastic constants of porous media [10–14]. These analyses fall into two categories: noninteracting models, in which influence of neighboring pores is neglected, and interacting models, which consider this influence. Some common methods, such as the self-consistent, differential and Mori-Tanaka schemes [15,16] are used in these analyses. Nakamura et al. [17] investigated effects of pores on mechanical properties of plasma sprayed  $\text{Al}_2\text{O}_3$ – $\text{TiO}_2$  coatings through detailed finite element models with geometries similar to these actual coatings containing many embedded pores, and minimum domain size to obtain consistent numerical results were estimated. All these previous studies provided useful information about fundamental characteristics and methodologies in micromechanical analysis of porous materials, however, an efficient and accurate computational tool for the correlation of effective thermal and mechanical properties and the “brick wall” microstructure of thermally sprayed TBCs has not yet been established. This is because of the lack of complete microstructural information in terms of orientation scatter, quantitative delineation of component porosities (interlamellar pores, intrasplat microcracks and globular pores in this case), and splat interfaces.

In this study, we develop a computationally based predictive capability for effective thermal conductivity and elastic modulus of plasma sprayed porous TBCs through two approaches. The two approaches include finite element analysis on a domain, obtained through experimentally derived collective microstructural information in one case and through quantification of real microstructural images in the other. The three tasks undertaken include firstly identifying the contribution of individual void components towards reduction of material properties, secondly evaluating the strength and weakness of each approach, and finally addressing the effect of splat boundaries. In each approach, four different feedstocks of zirconia powder are used to fabricate the coatings. In order to quantify the effect of splat boundaries, the other major microstructural contributor on the property determination, the coatings are thermal cycled, which simulates the mechanical system in oper-

ation. This process essentially eliminates splat interfaces, while many voids and pores remain intact. Although there is no doubt that splat interfaces provide additional reduction in the effective properties, accurate quantification of their effect has never been reported. With the thermal cycled coatings, our estimation approaches are again carried out to quantify the influence of the splat interfaces.

To model porous materials effectively, two important issues should be considered. First, the model sample must be large enough to contain sufficient microstructural features so that a *representative* thermal or mechanical response can be obtained. If the modeling volume is too small, the numerical results may not be the average due to the stochastic nature of the plasma-spray microstructure, and also because of numerical artifacts introduced at the boundaries. Second, detailed microstructural features must be included in the model to reflect the real microstructure of the coatings. These considerations were taken into account during the modeling procedures. In this paper, two distinctly different methods to model the porous coatings are introduced. They compliment each other with respect to the domain size and realistic nature of the microstructure. One of them features the artificial rebuilding of the porous structure based on the experimentally derived volumetrically averaged pore distributions obtained by the SANS studies. The other is an image-analysis based approach, which involves thresholding of real microstructure images (SEM/OOF).

## 2. Feedstock and fully dense properties of PSZ coatings

In the present study, our aim also involves examination of various material powder feedstock characteristics (such as particle density, size and shape) on the anisotropic void structure. The type of feedstock greatly affects the properties of fabricated zirconia coatings since they interact differently in a plasma flame and influence microstructural development. The two most influential factors, which are significant with regards to heat and momentum transfer, are the particle shape and

size. The influence of feedstock particle size on the microstructure and properties of zirconia coatings, in the case of varying particle shapes, has been reported by the authors elsewhere [18]. Four coatings investigated in this study are made from commercially available zirconia powders, all of which are partially phase-stabilized (PSZ) with 6–8 wt% yttria, but made by various manufacturing methods. They are classified as “fused and crushed” (F&C), “plasma densified hollow spheres” (HOSP), “sol–gel” and “sintered” feedstock. Although each is denoted as its own feedstock type, it is important to note that the materials tested here represent only one of many available varieties for each powder. The powders made by the F&C method produced angular/polyhedral particles with 10–60  $\mu\text{m}$  size. The plasma-densified HOSP process produced 20–120  $\mu\text{m}$  hollow spheres. These feedstocks produce a far greater density of splat interfaces in coatings than the other feedstocks and, thus significantly lower thermal conductivity. The sol–gel technique exhibited spherical/equiaxed morphology with 5–50  $\mu\text{m}$  size. The sintered technique produced 20–70  $\mu\text{m}$  globular/rough-textured particles. The feedstock morphologies are shown in Fig. 1.

Fig. 2 shows a polished and a fractured cross-section of a typical plasma sprayed PSZ coating. The polished cross-section observed under optical

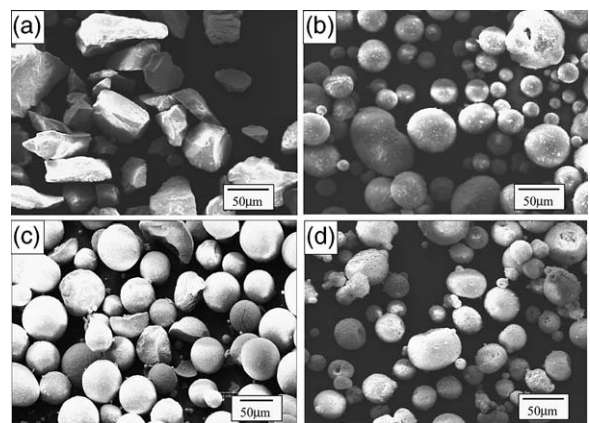


Fig. 1. Four different feedstock used for plasma sprayed coatings. (a) Fused and crushed (F&C): angular (10–60  $\mu\text{m}$ ). (b) HOSP: hollow spheres (20–120  $\mu\text{m}$ ). (c) Sol–gel: spherical (5–50  $\mu\text{m}$ ). (d) Sintered: spherical (20–70  $\mu\text{m}$ ).

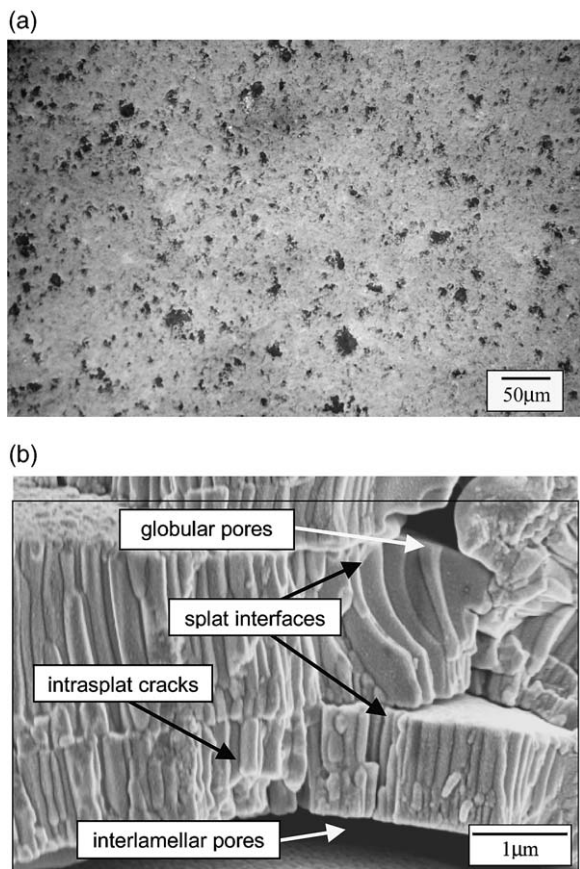


Fig. 2. Microstructure of PSZ coating prepared from fused and crushed (F&C) feedstock: (a) optical micrograph of a large domain; (b) SEM image showing detail microstructural features.

microscopy in Fig. 2(a) shows globular porosity. The interlamellar pores and intrasplat cracks remain unresolved at this magnification. The scanning electron microscopy (SEM) image in Fig. 2(b) shows splat–splat interaction where columnar grains are evident. Other features such as interlamellar pores, cracks and globular pores are also observed. The globular pores originate from gas entrapment and interlamellar pores due to improper adhesion at certain places. While well-adhered splats are observed for the deposit from the F&C feedstock, combinations of interlamellar pores, cracks and globular pores are abundant for the other coatings. Macroscopically, the coating from the sol–gel feedstock has numerous interla-

mellar pores compared with the others. The HOSP coating shows a larger number of unmelted particles, owing to the broad powder particle size distribution of this particular HOSP powder.

All types of coatings were evaluated for porosity content and property (thermal conductivity and elastic modulus) measurements. The porosity content was determined using the precision density method, where mass-over-volume ratios were obtained for a cut rectilinear specimen. The technique gives a fractional density (or porosity) uncertainty of standard deviation of  $\pm 1\%$  based on the average of 10 measured identical specimens and an assumed theoretical density of  $6 \text{ g/cm}^3$ . Thermal conductivity measurements were carried out at room temperature on a 12.5 mm (0.5 in.) diameter free-standing coating disk, coated with carbon, using a Holometrix laser flash thermal diffusivity instrument. In-plane and out-of-plane elastic moduli were measured for coatings bonded to the substrate, also at room temperature. Depth-sensitive indentation measurements were carried out with a Fischerscope 100C microhardness tester using a Vickers-type indenter (with a maximum load  $F_{max} = 1 \text{ N}$ ). The experimental results of the properties as well as the total porosity are shown in the Table 1. Here,  $K_L$  and  $E_L$  are the thermal conductivity and elastic modulus, respectively, in the spray direction and  $E_T$  is the modulus in the transverse direction. The exact values of properties for the bulk zirconia (6–8 wt% yttria partially stabilized) are difficult to obtain especially because its phase can be altered during plasma spraying processing. Here, the thermal conductivity of fully dense zirconia is assumed to be  $2.5 \text{ W/mK}$  based on a measured annealed electronic beam physical vapor deposition (EB-PVD) sample. This sample

Table 1  
Experimental values of effective properties and porosity

	Porosity (vol%)	$K_L$ (W/mK)	$E_L$ (GPa)	$E_T$ (GPa)
F&C	7.6	0.95	76	89
HOSP	12.2	0.64	48	47
Sol–gel	13.5	0.85	69	80
Sintered	15.0	0.89	72	89

is nearly free of pores and voids that would influence the properties in the deposition direction, and has the similar phase of zirconia as that in the coatings. However, it is expected that the true value may be slight higher since the annealed sample still contains minute amount of porosity and interfaces. Similar values can be found in [19,20]. For the fully dense coating, the elastic modulus is assumed to be 200 GPa at room temperature [21].

### 3. SANS approach

#### 3.1. SANS measurements

The SANS studies involve monochromatic neutrons passing through the specimen in transmission geometry and the scattered neutrons are recorded on a 2D detector. The scattering occurs at the void–grain interface due to differences in scattering length density between the material and the pores. The details of the experiment are described elsewhere (for example, [22,23]). The experiment involved two types of measurements. The first delivers the total void surface area per unit sample volume, independent of the precise void morphology. The fine features in the microstructure are major contributors to this deduced surface area. The second involves a measurement of the beam-broadening due to anisotropic multiple scattering of long wavelength neutrons. The multiple scattering usually arises from the coarse features in the microstructure. Thus combining the two derived results along with the total porosity in the system yield quantitative information of the microstructural features. The results include quantitative delineation of the three void components (interlamellar pores, intrasplat cracks and globular pores) in terms of their porosity contribution, the volume-weighted mean-opening dimensions of the intrasplat cracks and interlamellar pores, their orientation distributions with respect to the spray direction, and the diameters of the globular pores. Based on this input, a 2D finite element model is constructed as described in Section 3.2.

In the SANS measurement, it was assumed that the porosity is made up of three types of pores. These are, “Pores” (interlamellar pores), “Cracks”

(intrasplat cracks) and “Voids” (globular or irregular pores). These three components differ in mean size, size distributions, orientation distribution and morphology. All of the pore shapes are idealized to be spheroidal elements with aspect ratios of  $b/a = 1/5$  ( $a$  and  $b$  are major and minor axes) for Pores,  $b/a = 1/10$  for Cracks, and  $b/a = 1$  for Voids. Through the SANS measurements, volume ratios of different types of pores can be identified. Fig. 3 shows the constitution of porosity from the three types of pores for the four types of feedstock. The coating processed through the sintered technique has the highest total porosity, while the coating from F&C feedstock has the lowest. For all the cases, globular pores contribute the largest percentage of the total porosity, especially for the coating from the sintered feedstock, in which the fraction of globular pores is nearly 60% of the total porosity. Cracks have the lowest contribution in the total porosity for all the cases.

To generate the finite element model, the SANS measurements of the coatings’ microstructure are used as input. The experimental results, consisting of total void surface area, anisotropy and beam broadening, along with total porosity information, are obtained for quantitative analysis. The analysis provides the orientation distributions, the mean opening dimensions and the porosity contribution for each void system. We find interlamellar pores to be predominantly parallel to the substrate, while

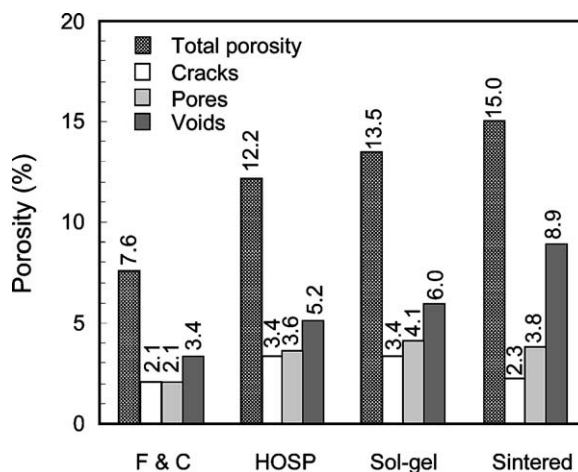


Fig. 3. Compositions of total porosity from three types of pores determined by the SANS measurements [21].

intrasplat cracks are predominantly perpendicular to the substrate. Since the cracks are generally finer than the interlamellar pores, the aspect ratio for the cracks is set to a smaller value (more oblate) than for the interlamellar pores. While the aspect ratios of the spheroidal elements are much milder than the true aspect ratios of the interlamellar pores and intrasplat cracks, the values above suffice for the respective populations of spheroidal voids assumed to form a space-filling network throughout each void system. Indeed, the relatively small area of each spheroidal element permits undulations in the true interlamellar pores and intrasplat cracks to be followed. Furthermore, it is the mean opening dimension,  $\langle \text{O.D.} \rangle = 4R/3$ , rather than the oblate disk diameter,  $2R$ , that is the physical dimension of interest. (In contrast, for the globular voids, the diameter fitted is associated with the actual mean globular pore diameter.) Hence, the mean opening dimension (typically in sub-microns) is used to calculate mathematical parameters of microstructural features. The distributions of pores are tabulated in Table 2 where the probabilities of orientations (divided into three angle ranges) and the assumed dimensions of pores are listed (voids are orientation independent). To artificially rebuild the

porous structure, volumetrically averaged SANS measurements were graphically represented in a matrix. For convenience, all of the pore shapes are idealized to be hexagonal with appropriate dimensions for the major and minor axes. The detailed steps to build a 2D porous model for the coating from the F&C feedstock are described next.

### 3.2. Modeling procedure

First, the sum of all types of pores is chosen to be 600 pores. In order to obtain an effective property that is model-independent, a sufficient number of pores must be included. However, a very large number can increase the computation effort. Based on an earlier analysis [17], 600 pores should be sufficient to produce stable results with a standard deviation  $< 2\%$ . Second, the total number of each pore type (i.e. pores, cracks, voids) is allocated based on the probabilities listed in Table 2. For the case of F&C, there are 375 cracks, 190 pores and 35 voids within the total porosity volume fraction of 7.6%. In addition, out of 375 cracks, 289 have the orientation angles between  $60^\circ$  and  $90^\circ$  to the transverse direction, 85 cracks for  $30^\circ$ – $60^\circ$ , one crack for  $0^\circ$ – $30^\circ$ . The orientation ranges

Table 2  
Pore morphology of coatings for different types of feedstock

	Probability (%)				$a$ ( $\mu\text{m}$ )	$b$ ( $\mu\text{m}$ )
	$0^\circ \leq \phi \leq 30^\circ$	$30^\circ \leq \phi \leq 60^\circ$	$60^\circ < \phi \leq 90^\circ$	Total		
<i>F&amp;C</i> (porosity: 7.6%)						
Cracks	0.2	14.2	48.1	62.5	0.528	0.053
Pores	28.0	2.2	1.5	31.7	0.528	0.106
Voids				5.8	0.687	0.687
<i>HOSP</i> (porosity: 12.3%)						
Cracks	0.3	14.0	47.6	61.9	0.670	0.067
Pores	27.8	4.2	0.8	32.8	0.670	0.134
Voids				5.3	0.872	0.872
<i>Sol-gel</i> (porosity: 13.5%)						
Cracks	0.5	13.1	45.2	58.8	0.679	0.068
Pores	31.8	2.4	0.8	35.0	0.679	0.136
Voids				6.2	0.883	0.883
<i>Sintered</i> (porosity: 15.0%)						
Cracks	0.3	10.7	36.7	47.7	0.610	0.061
Pores	37.6	2.7	1.0	41.3	0.610	0.122
Voids				11.0	0.793	0.793

are allocated similarly for pores as well. Third, a special computational code was developed to place these types of pores in a rectangular domain (with 3:5 ratio). Each pore location is chosen arbitrary with the random number generator in sequence. During the model construction, placements of pores are checked to avoid overlapping. For pores and cracks, their orientation ( $\phi$ ) is also randomly determined within the specific ranges. The final configurations of a typical pore morphology for the F&C feedstock is shown in Fig. 4(a) in a domain size of about  $30 \times 50 \mu\text{m}$ . It is important to note that although the model domain size is small, the pore morphology is the *representative* of an actual coating with  $\sim 1 \text{ mm}$  thickness (measured through the SANS technique). In addition, for the calculation of effective properties, only the relative sizes of pores matter and there is no size-scale in the solutions.

After the reconstruction of the porous structures,

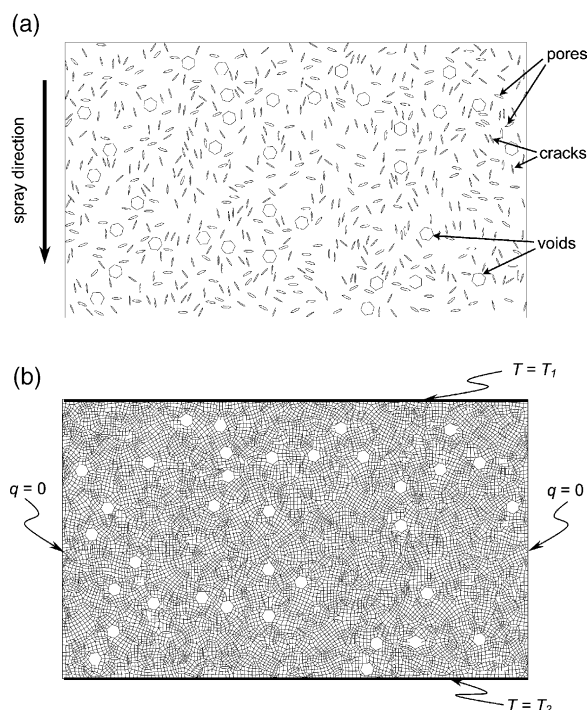


Fig. 4. SANS-based model of F&C coating used to estimate effective properties. The model dimensions are  $30 \times 50 \mu\text{m}$ . (a) Outlines of randomly placed pores. (b) Finite element mesh with boundary conditions: fixed temperatures at the top and bottom surfaces and insulated lateral sides.

a finite element mesh is generated using a mesh-generator code. Fig. 4(b) shows the mesh for the coating from the F&C feedstock, in which about 12,000 four-noded elements are used. Similar meshes are constructed for the other coatings. Once the modeling is complete, a standard finite element analysis is carried out to estimate the effective properties of these coating microstructures. The effective thermal conductivity is determined with the steady-state heat transfer analysis. To obtain the effective thermal conductivity along the spray direction, a fixed temperature condition is prescribed in both the top and the bottom boundaries, and the other two boundaries are considered as insulated boundaries, as shown in Fig. 4(b). Then, the effective thermal conductivity in the spray direction can be computed with Fourier's equation,

$$K_{\text{eff}} = \frac{QL}{W\Delta T} \quad (1)$$

Here,  $K_{\text{eff}}$  is the effective thermal conductivity,  $Q$  is the total steady-state heat flux per unit thickness through a transverse cross-section of the model,  $W$  and  $L$  are the width and height of the model, respectively, and  $\Delta T$  is the temperature difference between the top and bottom boundaries. Note that  $Q$  is constant for any transverse cross-sections under steady-state conditions. Since the thermal conductivity of air is very small ( $\sim 0.03 \text{ W/mK}$  at room temperature [24]) as compared to that of the bulk material, zero conductivity is assumed within void areas in our models. Similarly, the effective thermal conductivity in the transverse direction can also be calculated. The effective modulus was determined through the simulation of uniaxial tension for these models.

#### 4. SEM/OOF approach

The volumetrically averaged information in the SANS-based model does not account for the variations in pore sizes and shapes (apart from the three types), thus limiting its similarity with the real microstructure. The image analysis-based approach relies on the real microstructural images thus accounting for the above limitation. However, a compromise must usually be made between the

smallest sizes resolved and the sample domain size (as controlled by the microscope magnification). Also, problems can arise in interpreting fine anisotropic features that are partly out of the plane of view and detecting coarse features due to presence of pullouts generated during metallographic preparation. Direct 2D modeling of complex microstructures through image analysis became feasible in recent years [25]. The key element of the image analysis approach is to identify and model the realistic microstructural image instead of the volumetrically averaged microstructural features as in the SANS method. Here, a cross-section of the zirconia coating is captured with the SEM. The digitized image is turned into a finite element mesh using the object oriented finite (OOF) element method, which was developed by the National Institute of Standard and Technology. There are two steps in the process. First, components in the image must be identified and assigned appropriate material properties. Here, the area of image is chosen so that it does not contain pullout and unusually large pores. Second, the finite element mesh must be generated and refined until it represents sufficient microstructural details. Usually, this SEM/OOF approach is suitable for modeling a *smaller* domain compared to the SANS approach. A large domain with detailed microstructural features would require a large number of finite elements. However, a small domain may not represent the *averaged features* of the entire coating, and the result may vary depending upon the location of image. Alternatively, to obtain the effective properties of the entire coating, several local regions may have to be modeled separately, and the averaged result should be used. Furthermore, high graphic resolution is necessary to capture thin cracks, otherwise they do not appear in the image. Thus, for a given computational resource, the process usually requires a compromise between the domain size and the model resolution.

#### 4.1. SEM images

For obtaining the necessary cross-sectional images, the as-sprayed coatings were cut, mounted and polished using standard procedures for thermal

sprayed ceramic coatings. Vacuum impregnation is used while mounting to prevent major pullouts during metallographic preparation. SEM was used to obtain images at  $\times 500$  and higher using a FEG SEM (LEO 1550). The procedure adopted for image acquisition entailed a back-scattered electron imaging mode for higher contrast between pores and ceramic matrix, an accelerating voltage of 15–25 kV, a working distance of 8–9 mm and an image size of  $1024 \times 1024$  pixels. The use of SEM images as opposed to optical images ensures lesser errors through detection of pullouts and also a higher resolution for the fine cracks in the coating. These SEM images were then used for image analysis.

An SEM grayscale micrograph of the coating from the F&C feedstock, with the size of  $170 \times 170 \mu\text{m}$ , is shown in Fig. 5(a). This domain is in the middle area of the coating and should be considered a local region compared with the entire coating, whose thickness is about 1 mm. The darker areas in the image represent the pores.

#### 4.2. OOF procedure

The OOF program is designed to read pixels from this image file and group them according to their colors or grayscale levels. Each group stands for a specific constituent. In this case, by setting threshold pixel value, two groups are obtained for the pores and the matrix material, respectively. The threshold pixel value should be selected carefully in order that chosen pixel groups closely match the actual distribution of pores. After distinguishing the two phases, a finite element mesh is generated with this program. The elements near to the interfaces are refined and adjusted so that the interfaces are well described with element boundaries. The outline and mesh of the F&C specimen are shown in Fig. 5(b) and (c). There are a total of about 22,000 nodes and 39,000 triangular elements. Here, splat boundaries are not modeled since their thickness is near zero, and are difficult to resolve from micrographs at this magnification. The porosity volume fraction of this model, obtained from image analysis thresholding, is 7.4%. This is slightly lower than the porosity obtained by precision density method (7.6%), which is input into

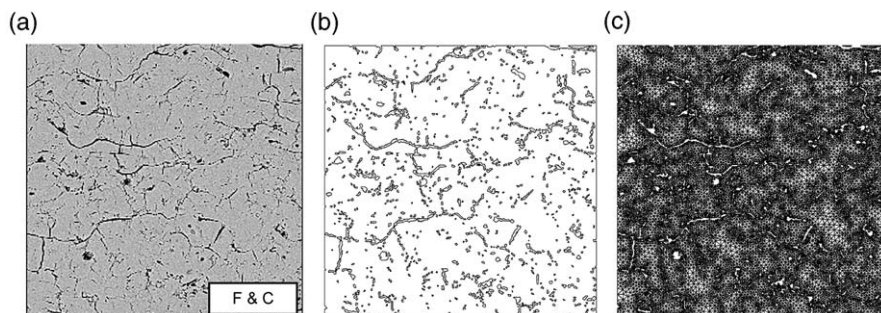


Fig. 5. Model construction in the SEM/OOF approach. (a) SEM image ( $170 \times 170 \mu\text{m}$ ) of F&C specimen with darker area representing pores. (b) Outline of pores generated from the micrograph with 7.4% local porosity. (c) Finite element mesh.

the SANS model. Although this difference is well within the measurement variation, there can be two reasons to explain the difference. First, since the domain of the SEM/OOF based model only stands for a small region in the coating, this porosity should be considered as a local value instead of the overall porosity. Thus it varies from selected image to image. Second, due to the limited resolution of micrograph, some very thin cracks, not shown in the image, cannot be modeled here, while these thin cracks can still be detected through the SANS measurement. Using the similar modeling approach, the SEM/OOF models of the other three coatings are generated, as shown in Fig. 6. Their

local porosities are also slightly smaller than the precision density method values. After the meshes are constructed, the effective thermal conductivity and elastic modulus are estimated through the same finite element procedure used for the SANS approach.

## 5. Estimated properties

Before reporting the effective properties, a *transient* heat transfer analysis is carried out to illustrate the heat flow process within the porous coatings. Figs. 7 and 8 show the temperature and heat

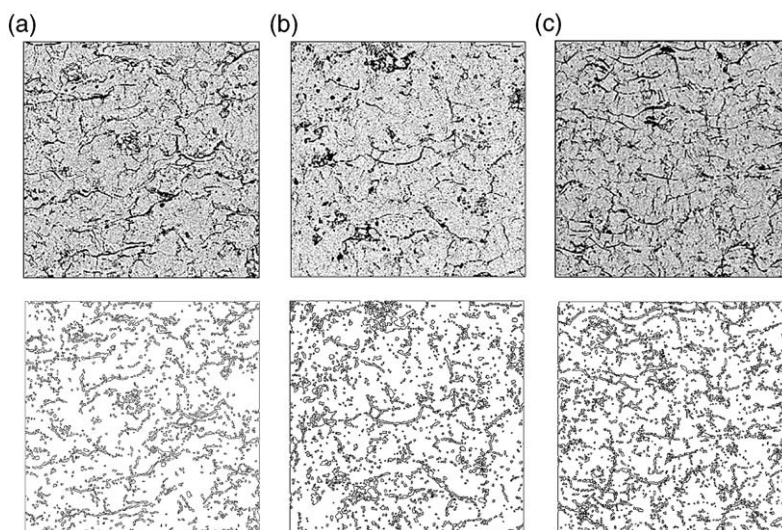


Fig. 6. SEM images ( $170 \times 170 \mu\text{m}$ ) and pore outlines for SEM/OOF models of other coatings; (a) HOSP, local porosity is 10.8%, (b) sol-gel, 13.3%, (c) sintered, 14.1%.

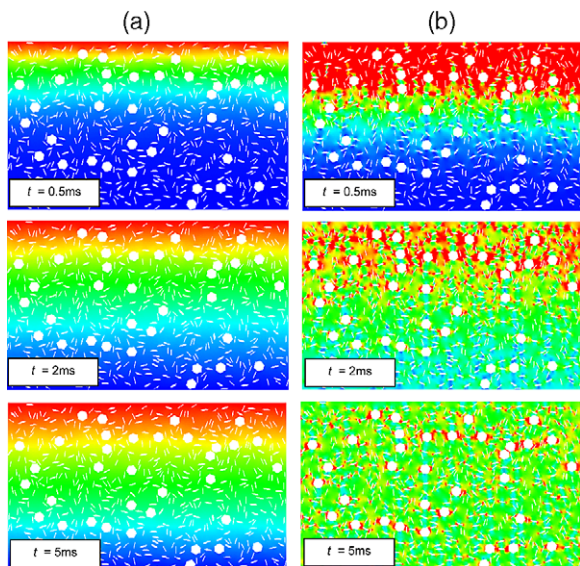


Fig. 7. Transient temperature and heat flux of SANS model for sol-gel coating. The model size is  $30 \times 50 \mu\text{m}$ . (a) Temperature profile, red color indicates high temperature. (b) Heat flux profile, red color indicates high heat flux. Heat flux is higher at narrow passages.

flux evolution of the coating made from the sol-gel feedstock with the SANS-based model and SEM/OOF-based model, respectively. For both approaches, the temperature is imposed at the top surface and the heat flows downward. Initially, a very large heat flux is observed near the top, but as time progresses, it propagates through the coatings. The temperatures at the top and bottom surfaces are maintained at constant levels. After some time, the steady-state condition is reached. Note, the thermal diffusivity of the PSZ is assumed as  $600 \text{ J/kg K}$  [19]. The time to reach the steady-state depends on the size of the model. For the SANS model, it is about  $t = 5 \text{ ms}$  with  $L = 30 \mu\text{m}$ , and for the SEM/OOF model it is about  $t = 30 \text{ ms}$  with  $L = 170 \mu\text{m}$ . In both cases, the heat flux contours clearly illustrate the effect of pores. There are concentrations of the heat flux (i.e. high heat flow rate) between neighboring pores. Where the spaces between pores are narrow, the flux increases (shown with red), while less heat flows are shown at above and below some large pores (green to blue). In general, greater variations of heat flux

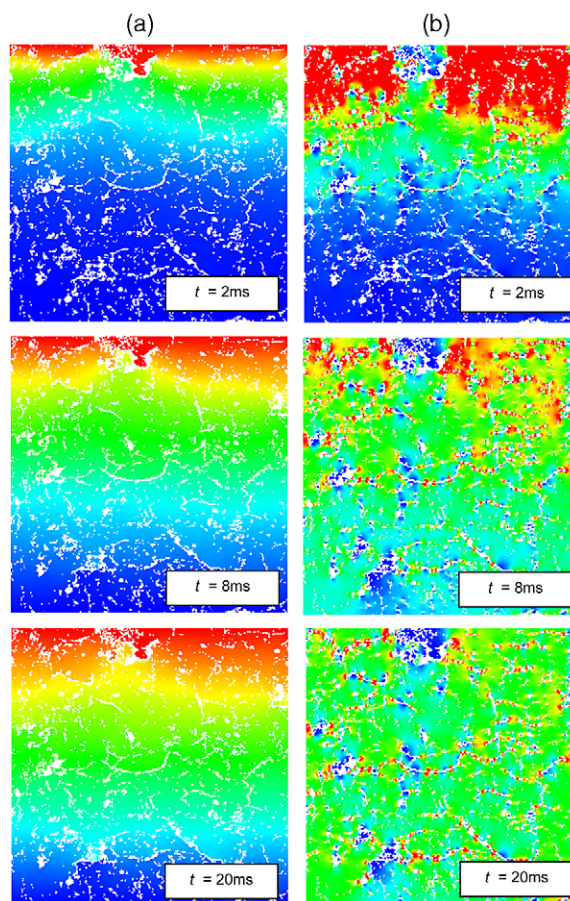


Fig. 8. Transient temperature and heat flux of SEM/OOF model for the sintered coating. The model dimensions are  $170 \times 170 \mu\text{m}$ . (a) Temperature profile, red color indicates high temperature. (b) Heat flux profile, red color indicates high heat flux.

within the domain correspond to lower effective thermal conductivity.

The effective thermal conductivity is obtained from a *steady-state* heat transfer analysis. The estimated values are tabulated in Tables 3 and 4 for the SANS- and SEM/OOF-based models, respectively. In addition, the results of elastic modulus, obtained through static uniaxial loading calculations, are shown in the same tables. In each model, the results along transverse direction are obtained by rotating the boundary conditions. Here, the fully dense thermal conductivity and elastic modulus of the bulk material are chosen as  $K = 2.5 \text{ W/mK}$  and  $E = 200 \text{ GPa}$ , respectively.

Table 3  
Estimated effective properties based on SANS approach

	Porosity (%)	$K_L$ (W/mK)	$K_T$ (W/mK)	$E_L$ (GPa)	$E_T$ (GPa)
F&C	7.6	2.02	1.94	146	135
HOSP	12.2	1.78	1.68	119	107
Sol-gel	13.5	1.72	1.64	113	104
Sintered	15.0	1.69	1.68	111	111

Table 4  
Estimated effective properties based on SEM/OOF approach

	Porosity (%)	$K_L$ (W/mK)	$K_T$ (W/mK)	$E_L$ (GPa)	$E_T$ (GPa)
F&C	7.4	1.86	2.04	123	149
HOSP	10.8	1.73	1.93	113	135
Sol-gel	13.3	1.62	1.70	105	109
Sintered	14.1	1.50	1.69	92	110

The effective properties calculated through both approaches decrease with increased total porosity. The coating prepared from the F&C feedstock has the lowest porosity in the four systems, and the highest effective properties. The coatings from the sol-gel and sintered feedstock have lower properties due to higher porosities. The estimated effective properties as well as the corresponding experimental values are also shown in Fig. 9. (Note the laser flash instrument has not been used to determine the thermal conductivity in the transverse direction.) All of the estimated values are significantly higher than those of experimental results. For the thermal conductivity, the models estimated 20–40% drops from the fully dense value while the measured values range 62–74% off from the fully dense value. The discrepancy is greatest with the HOSP case, where the experimental values are less than half of the calculated values in both the SANS and SEM/OOF results. This difference can be attributed to the unusually large density of splat boundaries [23], which are not included in the modeling. For the Young's modulus, the discrepancies between the measured and estimated values are somewhat smaller. Each model shows larger drops from the bulk value as compared to the thermal

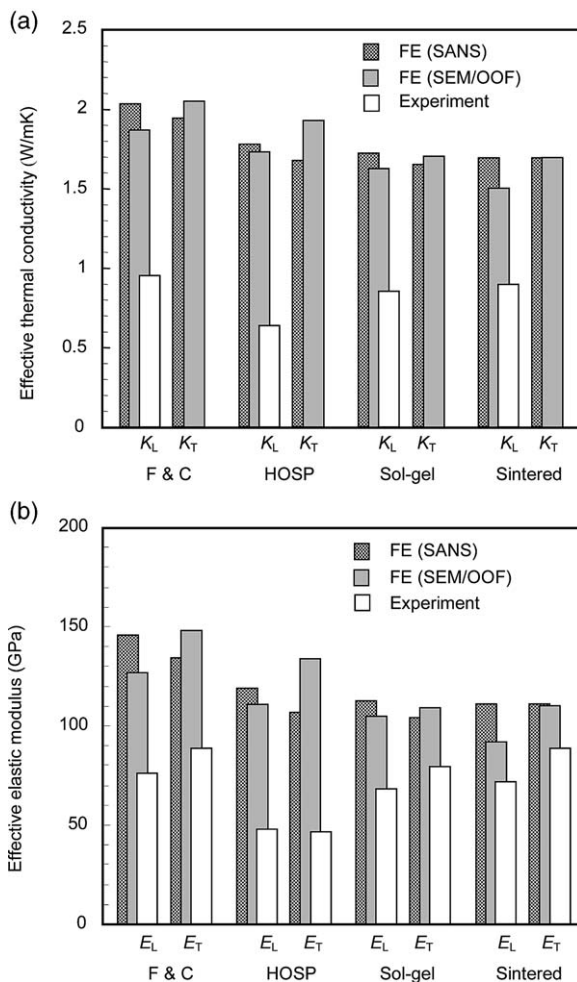


Fig. 9. Comparison of estimated and measured results along spray and transverse directions. (a) Effective thermal conductivity. (b) Effective elastic modulus.

conductivity results. The models estimated 26–54% drops from the bulk value while the measured values range 55–76% off from the bulk. Again, the largest discrepancy shows up with the HOSP feedstock. However, the estimated values are within 20–40 GPa of the experimental values for the sintered feedstock.

The anisotropic effects can be also observed in the elastic modulus shown in Fig. 9(b), where measured and estimated properties along both the spray and transverse directions are available. In general, the modulus is known to be greater along the transverse due to the pore morphology and the struc-

tures of splats. This is accurately simulated with the SEM/OOF models, which are consistent with the experimental results. Note, for the case of HOSP feedstock, almost no anisotropy is observed from the measurement. However, in each case, the SANS approach estimates a larger modulus along the spray direction. This discrepancy can be explained by the assumed size and aspect ratio for each classification of pores. Although they reflect the averaged morphology, the discrepancy may arise when large pores, such as very long interlamellar pores, are not modeled correctly. A long pore can cause a much larger drop in effective properties than shorter pores. Furthermore, the distributions of pore orientations are not assigned precisely, which may also cause inaccuracy. The SANS approach also includes intrasplat cracks, which can be detected through SANS technology, but cannot be fully identified through the image analysis due to their thinness. Since these intrasplat cracks are generally vertically oriented, they cause larger drops in modulus along the transverse direction. On the other hand, the pore modeling based on real images in the SEM/OOF approach takes into account long pores/cracks with precise orientations. This probably allowed more consistent anisotropic behavior to be estimated. The comparison of the two approaches is also shown in Fig. 10, where effective properties are shown with

functions of coating porosity. The experimental values are also included for reference (except for  $K_T$  where the measurement is not available). In each case, the property shows nearly linear variation with the porosity for the SANS and SEM/OOF approaches. Again, the HOSP case is anomalous due to its unusually high density of splat interfaces.

## 6. Effects of splat boundaries—thermal cycled coatings

As discussed earlier, it is probable that splat boundaries are major contributors in defining the properties of PSZ coatings. Based on the results shown in Section 5, out of the total decreases in the effective properties (i.e. the differences between the bulk and measured properties), approximately *half* are caused by the pores (e.g. ~40% for HOSP and ~75% for sintered cases). The remaining decrease should come from the presence of splat boundaries and other factors. Up to now, property information on splat–splat interfaces has been limited, and how they influence the heat flow and the stress transfer across the interfaces is unknown. We have initiated a probe into the characteristics of splat boundaries using high-resolution *transmission electron microscopy*. How-

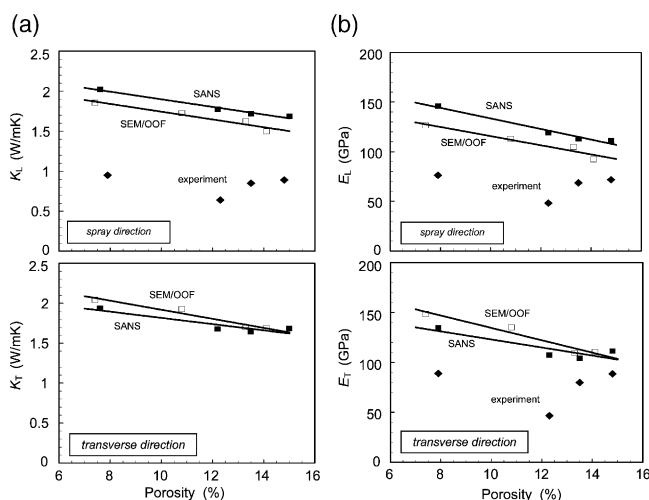


Fig. 10. Effective properties along spray and transverse directions are plotted as functions of porosity. (a) Effective thermal conductivity. (b) Effective modulus.

ever, at the moment, the splat boundaries cannot be physically modeled into either the SANS or SEM/OOF approach since their mechanical properties cannot be defined. Therefore, to identify the contribution of splat boundaries to the coating properties, we circumvent modeling splat boundaries by investigating similar coatings, but without splat interfaces. In order to eliminate splat boundaries, plasma sprayed coatings are thermal cycled. Within the thermal cycled samples, the only factor which influences the effective properties is the pore system. By comparing the results of as-sprayed coatings and thermal cycled samples, the effects of splat boundaries in principle can be quantified.

The thermal cycling treatment involves 10 cycles in which each cycle consists of two steps. First, heating the coatings to 1150 °C for 30 min. Second, subsequent cooling to room temperature for 15 min and heating again. Thermal cycling causes microstructural changes upon heating. Mainly, the splat boundaries and the thin intrasplat cracks are affected early on, since they tend to disappear. During the cycle, some large cracks also develop within the coatings due to CTE mismatch between the coating, the bond coat layer and the substrate. This causes the total porosity to be slightly larger than that of the as-sprayed coating. However, these macro-cracks are generally oriented vertically, and should have small influences on the spray direction property. The measured thermal conductivity values in the spray direction of the four thermal cycled coatings are listed in Table 5. They are substantially higher than those of corresponding as-sprayed coatings, listed in Table 1. Without the splat boundaries, the conductivities more than double in the thermal cycled coatings

and these results alone confirm the significant effect of splat interfaces.

Since some large cracks have been generated in the thermal cycled samples, and it is difficult to distinguish them from regular pore/cracks through the SANS measurement, only the SEM/OOF-based models are generated and analyzed to estimate the effective thermal conductivity of the thermal cycled coatings. The SEM images and pore outlines of the four thermal cycled coatings are shown in Fig. 11. The images show the existence of various pores and confirm that the thermal cycling process does not have a large influence on the pore morphology of coatings. The domain sizes are  $170 \times 170 \mu\text{m}$ , and about 40,000 triangle elements are used in each finite element mesh. The estimated effective thermal conductivities along the spray direction determined from the finite element analysis are listed in Table 5. In these calculations, the fully dense conductivity is still chosen as 2.5 W/mK. We can observe that for the thermal cycled samples, the computed  $K_L$  values are much closer to the corresponding experimental results compared with the case of as-sprayed coatings. In fact, the SEM/OOF results underestimate the measured values, with the biggest difference being in the case of sintered feedstock, for which the calculated result is about 25% lower than the measured result. This difference can be attributed to two factors. One is the inherent domain dependence of the SEM/OOF modeling approach (i.e. different domains may show different effective properties). The other is the choice of the fully dense conductivity in the calculation. As alluded to earlier,  $K = 2.5 \text{ W/mK}$  as obtained from the annealed EB-PVD sample may be smaller than the actual value. A higher value of  $K$  would give better agreement with the measured values. Nevertheless, the results shown in Fig. 12 clearly attest to the accuracy of our modeling approach to estimate the effective properties when the only major defining factor is porosity. Alternatively, the significance of splat interfaces on the overall property is illustrated from the additional analysis on the thermal cycled coatings. Also, the calculated results of thermal cycled coatings are close to those of corresponding as-sprayed coatings estimated by both the SEM/OOF and SANS approaches. The effect of splat bound-

Table 5  
Effective thermal conductivity for thermal cycled coatings based on SEM/OOF approach

	Porosity (%)	$K_L$ (W/mK) (measured)	$K_L$ (W/mK)	$K_T$ (W/mK)
F&C	7.2	2.14	1.94	2.08
HOSP	11.9	1.57	1.53	1.78
Sol-gel	11.2	1.91	1.65	1.81
Sintered	14.4	2.03	1.50	1.62

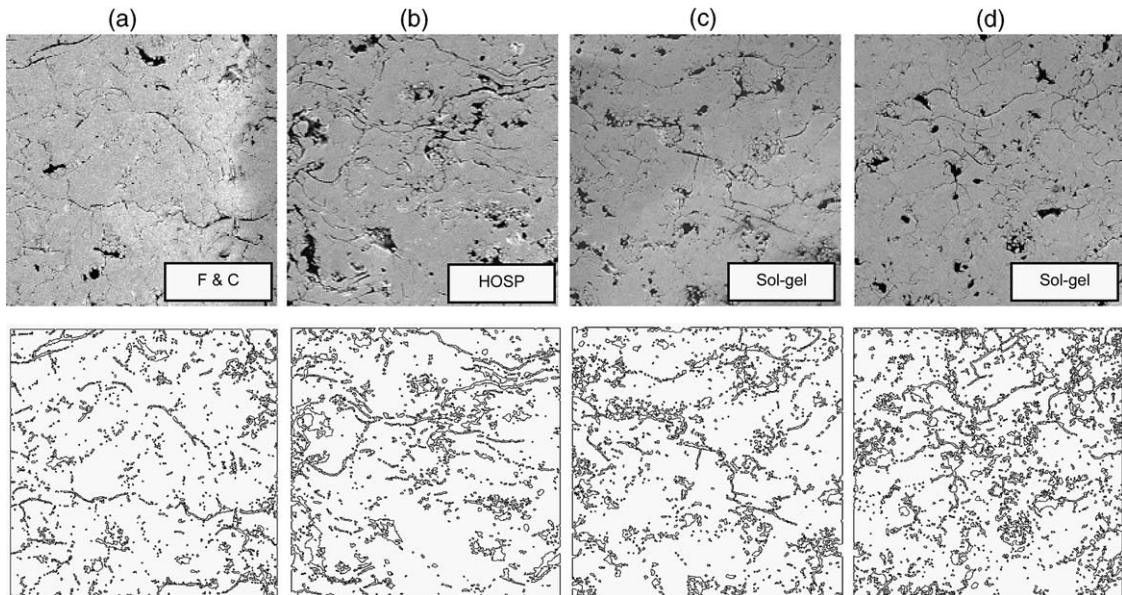


Fig. 11. Thermal cycled coatings for SEM/OOF approach ( $170 \times 170 \mu\text{m}$ ): (a) F&C local porosity is 7.2% (as-sprayed porosity: 7.4%), (b) HOSP, 11.9% (10.8%), (c) sol-gel, 11.2% (13.3%), (d) sintered, 14.4% (14.1%).

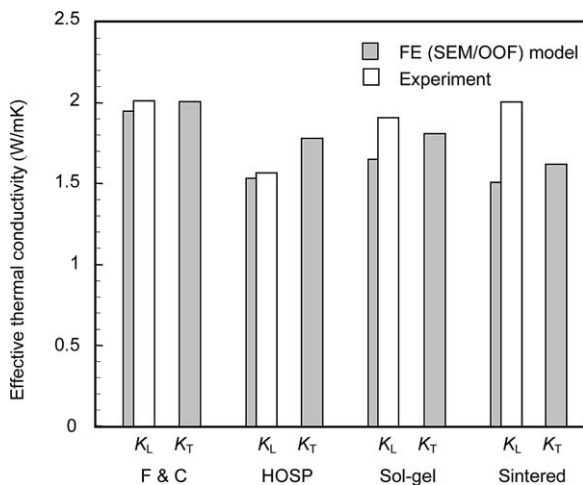


Fig. 12. Comparison of estimated (by the SEM/OOF approach) and measured effective thermal conductivity for thermal cycled coatings.

aries is unique for each different feedstock. For the HOSP case, the splat boundaries probably have the largest contribution to the total property reduction (of the as-sprayed coating), as its discrepancy with the model estimate is reduced most significantly with the thermal cycled coating.

## 7. Discussions

Effective thermal conductivity and elastic modulus of thermally sprayed PSZ coatings are estimated using two distinctly different modeling approaches. Both approaches identify the influence of various void components of the coatings, but with different interpretations. The SANS-based approach offers more consistent global averaging of pore morphology of the entire coating, while the image-based SEM/OOF approach provides more realistic simulation of pore morphology at a local region. Four PSZ coatings prepared from different feedstocks are investigated with both approaches. Porous microstructure causes considerable reduction of effective thermal conductivity and modulus in both the spray and transverse directions. The reduction increases with the total porosity. Generally, the pores account for 40–75% of the reduction in the effective properties, depending upon the feedstock and the fabrication process. Of the feedstocks tested, the relative pore effects are the largest with the sintered feedstock and the smallest with the HOSP feedstock. Our comprehensive analysis also elucidated that the relative effects of pores on the thermal conduc-

tivity and the elastic modulus to be not equivalent. With an identical porous model, a larger reduction is observed in the modulus than that in the conductivity from the finite element results.

Our study also finds the anisotropic effects to be relatively small for the plasma sprayed PSZ coatings. The property differences along the spray and transverse directions are about 2–8% for the current specimens. The SEM/OOF approach has shown more consistent anisotropic behavior relative to the experimental observations than does the SANS approach.

The effects of splat boundaries are estimated through the investigation of thermal cycled coatings. The SEM/OOF-based simulations yielded estimated values close to the measured values. This study enabled the effects of splat interfaces to be quantified for the first time. It appears that the splat interfaces account for 25–60% of the total reduction in the effective properties with larger contributions for coatings with high splat interface densities (e.g. HOSP coatings). It is important to note that the splat interfaces are as equally important as the porosity in defining the properties of plasma sprayed coatings. Furthermore, the splat interfaces may have greater influences on the thermal conductivity than on the elastic modulus. Their role as barriers to heat transmission may be more significant barrier to force transfer. Additional experimental measurements are required to verify the exact nature of splat interface role in the plasma sprayed coatings.

## Acknowledgements

The authors gratefully acknowledge the support of the US Army Research Office under grant DAAD19-02-1-0333 and the National Science Foundation MRSEC program at the SUNY at Stony Brook under grant # DMR-0080021. The authors also wish to thank Andrew Allen of the ceramics division at National Institute of Standards and Technology for help with SANS measurements.

## References

- [1] Herman H. Plasma-sprayed coatings. *Sci Am* 1988;259(3):112–7.
- [2] Herman H, Shankar NR. Survivability of thermal barrier coatings. *Mater Sci Eng* 1987;88:69–74.
- [3] Padture NP, Gell M, Jordan EH. Thermal barrier coatings for gas-turbine engine applications. *Sci Compass* 2002;296:280–4.
- [4] Markov K, Preziosi L. Heterogeneous media: micromechanics modeling methods and simulations. Birkhäuser Boston: c/o Springer-Verlag New York, Inc, 1999.
- [5] Kaviany M. Principles of heat transfer in porous media, 2nd ed. Springer-verlag New York Inc, 1995.
- [6] Kroupa F, Kachanov M. Effect of microcracks and pores on the elastic properties of plasma sprayed materials. In: Proceedings of the 19th Riso International Symposium on Materials Science: Modelling of Structure and Mechanics of Materials from Microscale to Product, Roskilde. 1998. p. 325–30.
- [7] Sevostianov I, Kachanov M. Modeling of the anisotropic elastic properties of plasma-sprayed coatings in relation to their microstructure. *Acta Mater* 2000;48:1361–70.
- [8] Leigh SH, Berndt CC. Modelling of elastic constants of plasma spray deposits with ellipsoid-shaped voids. *Acta Mater* 1999;47:1575–86.
- [9] Leigh SH, Berndt CC. Quantitative evaluation of void distributions within a plasma-sprayed ceramic. *J Am Ceramic Soc* 1999;82(1):17–21.
- [10] Zhao YH, Tandon GP, Weng GJ. Elastic moduli for a class of porous materials. *Acta Mech* 1989;76:105–30.
- [11] Zhao YH, Weng GJ. Effective elastic moduli of ribbon-reinforced composites. *J Appl Mech, Trans ASME* 1990;57(1):158–67.
- [12] Argyris J, Doltsinis Ist, Eggers M, Handel R. Studies on ceramic coatings, deduction of mechanical and thermal properties from the microstructure of the material. *Comput Methods Appl Mech Eng* 1994;111:203–34.
- [13] Kachanov M, Tsukrov I, Shafiro B. Effective moduli of solids with cavities of various shapes. *Appl Mech Rev* 1994;47:S151–S74.
- [14] Kachanov M. Elastic solids with many cracks: a simple method of analysis. *Int J Solids Struct* 1987;23:23–43.
- [15] Hashin Z. The differential scheme and its application to cracked materials. *J Mech Phys Solids* 1988;36:719–34.
- [16] Christensen RM. A critical evaluation for a class of micromechanical models. *J Mech Phys Solids* 1990;38:379–404.
- [17] Nakamura T, Qian G, Berndt CC. Effects of pores on mechanical properties of plasma-sprayed ceramic coatings. *J Am Ceramic Soc* 2000;83(3):578–84.
- [18] Kulkarni A, Vaidya A, Goland A, Sampath S, Herman H. Processing effects on porosity–property correlations in plasma sprayed yttria-stabilized zirconia coatings. *Mater Sci Eng A* 2003;359(1-2):100–111.
- [19] Hasselman DPH, Johnson LF, Bentsen LD, Syed R, Lee HL, Swain MV. Thermal diffusivity and conductivity of

- dense polycrystalline ZrO<sub>2</sub> ceramics: a survey. *J Am Ceramic Soc* 1987;66(5):799–806.
- [20] Schlichting KW, Padture NP, Klemens PG. Thermal conductivity of dense and porous yttria-stabilized zirconia. *J Mater Sci* 2000;36:3003–10.
- [21] Ruh R, Mazdiyasi KS. Young's modulus, flexural strength, and fracture of yttria-stabilized zirconia versus temperature. *J Am Ceramic Soc* 1997;80(4):903–8.
- [22] Allen A, Ilavsky J, Long GG, Wallace J, Berndt C, Herman H. Microstructural characterization of yttria-stabilized zirconia plasma-sprayed deposits using multiple small-angle neutron scattering. *Acta Mater* 2001;49:1661–75.
- [23] Kulkarni A, Wang Z, Nakamura T, Sampath S, Goland A, Herman H et al. Comprehensive materials characterization and predictive property modeling of plasma sprayed zirconia coatings. *Acta Mater* 2003;51:2457–75.
- [24] Lima JAP, Marin E, da Silva MG, Sthel MS, Schramm DU, Cardoso SL et al. Characterization of the thermal properties of gases using a thermal wave interferometer. *Meas Sci Tech* 2001;12:1949–55.
- [25] Langer SA, Fuller Jr. ER, Carter WC. OOF: an image-based finite-element analysis of material microstructures. *Comput Sci Eng* 2001;3(3):15–23.